Bioactive Materials 25 (2023) 176–188

Contents lists available at ScienceDirect

Bioactive Materials

journal homepage: www.keaipublishing.com/en/journals/bioactive-materials

Early osteoimmunomodulation by mucin hydrogels augments the healing and revascularization of rat critical-size calvarial bone defects

Song Chen [a,1], Huan Wang [a,1], Dachuan Liu [a], Jianzhong Bai [a], Håvard Jostein Haugen [b], Bin Li [a,*], Hongji Yan [c,d,e,**]

[a] Orthopedic Institute, Department of Orthopedic Surgery, The First Affiliated Hospital, School of Biology & Basic Medical Sciences, Suzhou Medical College, Soochow University, Suzhou, Jiangsu, China
[b] Department of Biomaterials, Institute for Clinical Dentistry, University of Oslo, PO Box 1109 Blindern, Oslo, 0376, Norway
[c] AIMES - Center for the Advancement of Integrated Medical and Engineering Sciences at Karolinska Institute and KTH Royal Institute of Technology, 171 77, Stockholm, Sweden
[d] Department of Neuroscience, Karolinska Institute, 171 77, Stockholm, Sweden
[e] Division of Glycoscience, Department of Chemistry, School of Engineering Sciences in Chemistry, Biotechnology and Health, KTH Royal Institute of Technology, AlbaNova University Center, 106 91, Stockholm, Sweden

ARTICLE INFO

Keywords:
Mucin hydrogels
Monetite
osteoimmunomodulation
Bone
Revascularization

ABSTRACT

The design principle of osteogenic bone grafts has shifted from immunological inertness to limiting foreign body response to combined osteoimmunomodulatory activity to promote high-quality endogenous bone regeneration. Recently developed immunomodulatory mucin hydrogels have been shown to elicit very low complement activation and suppress macrophage release and activation after implantation *in vivo*. However, their immunoregulatory activity has not yet been studied in the context of tissue repair. Herein, we synthesized mucin-monetite composite materials and investigated their early osteoimmunomodulation using a critical-size rat bone defect model. We demonstrated that the composites can polarize macrophages towards the M2 phenotype at weeks 1 and 2. The early osteoimmunomodulation enhanced early osteogenesis and angiogenesis and ultimately promoted fracture healing and engraftment (revascularization of the host vasculature) at weeks 6 and 12. Overall, we demonstrated the applicability of mucin-based immunomodulatory biomaterials to enhance tissue repair in tissue engineering and regenerative medicine.

1. Introduction

Large calvarial bone defects (critical size) are often caused by trauma or cancer and fail to heal independently [1,2]. Autologous bone grafting has been the gold standard treatment approach for bone regeneration in the clinic [3,4]. However, this approach is often limited because of insufficient supply and secondary morbidity at the donor site [5,6]. Synthetic bone grafts have been proposed as an alternative to guide endogenous bone regeneration through the ossification mechanism [7–10]. The pioneering concept of osteoimmunology has shifted to the design principle of synthetic bone grafts with osteoimmunomodulatory activity, which promotes neobone formation and maturation rather than only limiting foreign body response and inducing osteogenesis [11–13]. These benefits could potentially be achieved through the careful development of biomaterials with integrated osteoimmunomodulatory and osteogenic functions that allow the biomaterial to direct the immune system to promote bone tissue repair [14]. During biomaterial-driven endogenous bone regeneration, the importance of macrophages has been recognized due to their plasticity at various phases of the healing process. M2-like macrophages, which are regulatory and anti-inflammatory, promote essential regenerative functions, including reducing inflammation and promoting osteogenic differentiation of stem cells [15–17]. Biomaterials designed to skew macrophages toward predominantly M2-like macrophages, away from the

Peer review under responsibility of KeAi Communications Co., Ltd.
* Corresponding author.
** Corresponding author. AIMES - Center for the Advancement of Integrated Medical and Engineering Sciences at Karolinska Institutet and KTH Royal Institute of Technology, 171 77, Stockholm, Sweden.
E-mail addresses: binli@suda.edu.cn (B. Li), hongji.yan@ki.se, hongji@kth.se (H. Yan).
[1] The authors contributed equally to the paper.

https://doi.org/10.1016/j.bioactmat.2023.01.022
Received 17 November 2022; Received in revised form 8 January 2023; Accepted 29 January 2023

pro-inflammatory M1 phenotype, can accelerate the bone healing process. Otherwise, persistent immune activation leads to chronic inflammation and bone degeneration. Previous studies have shown that the incorporation of immunologically active molecules is an efficient way of modulating the immune response of inorganic materials in a favorable direction [18,19]. Haugen et al., [20] and Liu et al., [21] have developed magnesium-modified hybrid materials capable of modulating early osteoimmunomodulation and promoting osteogenesis. Similarly, β-tricalcium phosphate functionalized with heparin induced M2 polarization and enhanced osteogenic differentiation of mesenchymal stem cell [22,23].

Mucin glycoproteins and mucin-derived hydrogels are another vital component of the immunoregulatory arsenal [24,25]. Mucins, bottlebrush macromolecules, are expressed as secreted forms that constitute the apical mucus on the epithelium or as transmembrane glycoproteins that form part of the glycocalyx [26]. Mucins share common densely glycosylated serine- and threonine-rich regions, with the O-linked glycans mostly ending with sialic acids and fucose residues [27]. Mucin glycans can interact with several types of cell surface receptors and modulate cellular response. For instance, secreted MUC2 mucins from various species attenuate lipopolysaccharide (LPS)-activated dendritic cells by interacting with their mucin glycans via galectin-3 receptor proteins [28]. Other sugar residues, such as sialic acids, interact with the Siglec family of receptors expressed on innate and adaptive immune cells [29]. Our previous study showed that mucin hydrogels elicit very mild complement activation, as evidenced by their activation of significantly low levels of the complement activation products C3a and C5b-9 protein fragments [30], and evade foreign body response *in vivo* by attenuating immune cell recruitment and activation [31]. Moreover, we also showed that terminal sialic acids on mucin hydrogels interact with macrophage receptors and modulate their activation [32,33]. However, the applicability of immunomodulatory mucin hydrogels in tissue repair and regenerative medicine remains unknown.

Among synthetic bone grafts, bioactive ceramics, especially calcium phosphate-based bioceramics, have been developed with different compositions. These materials are osteoconductive and osteoinductive, thereby serving as templates for bone growth and inducing endogenous bone regeneration, respectively [34,35]. Monetite ($CaHPO_4$, DCPA) is an acidic calcium phosphate that has been proven to have osteogenic potential *in vitro* and *in vivo* [36,37]. Compared to other calcium phosphates such as hydroxyapatite ($Ca_{10}(PO_4)_6(OH)_2$, HAp) and brushite ($CaHPO_4{\bullet}2H_2O$, DCPD), monetite is more resorbable under physiological conditions, which is promising to enhance endogenous bone fracture healing in orthopedic and orthodontic applications [38]. Monetite with tuned morphology and porosity has been obtained by dehydration of brushite or direct precipitation through wet chemical methods [39,40] and can be tailored and applied as an injectable cementitious paste or granules [41]. Monetite granules have been shown to improve bone regeneration in alveolar bone defects in humans [42] and critical calvarial bone defects in rabbits [43].

In this study, to investigate the osteoimmunomodulatory effect of mucin gels in fracture healing, we prepared mucin gel-monetite granule composite materials and implanted the grafts or monetite granules alone into a rat calvarial bone defect (critical size) (Scheme 1). Early osteoimmunomodulation by the grafts with mucin gel was investigated, which promoted earlier osteogenesis and angiogenesis compared to grafts without mucin gel. The phenotypes of infiltrated macrophages in the defect sites were assessed by immunofluorescence. Secretion of cytokines such as interleukin (IL)-8 and IL-1Ra, the expression of Runx2 and Sox9 and alkaline phosphatase (ALP) activity were studied for early osteogenesis. CD31, alpha-smooth muscle actin (α-SMA), and factor XIII were assessed for early angiogenesis. Finally, we studied the formation and maturation of the neobone through micro-computed tomography (Micro-CT), histology, immunohistochemistry, and optical photothermal infrared (O-PTIR) microscopy. Taken together, this work has shown that early osteoimmunomodulation by mucin-monetite composite materials resulted in augmented fracture healing and engraftment, demonstrating the applicability of mucin-based immunomodulatory biomaterials in tissue engineering and regenerative medicine.

2. Results and discussion

Porous architecture design plays an essential role in tissue engineering by providing nutrition and channels for cells to grow and migrate [44]. Calcium phosphates are ideal materials to act as porous templates for new bone formation. Despite of the good osteoconductivity and osteoinductivity of monetite, porous monetite materials have not been extensively studied [45]. Moreover, the

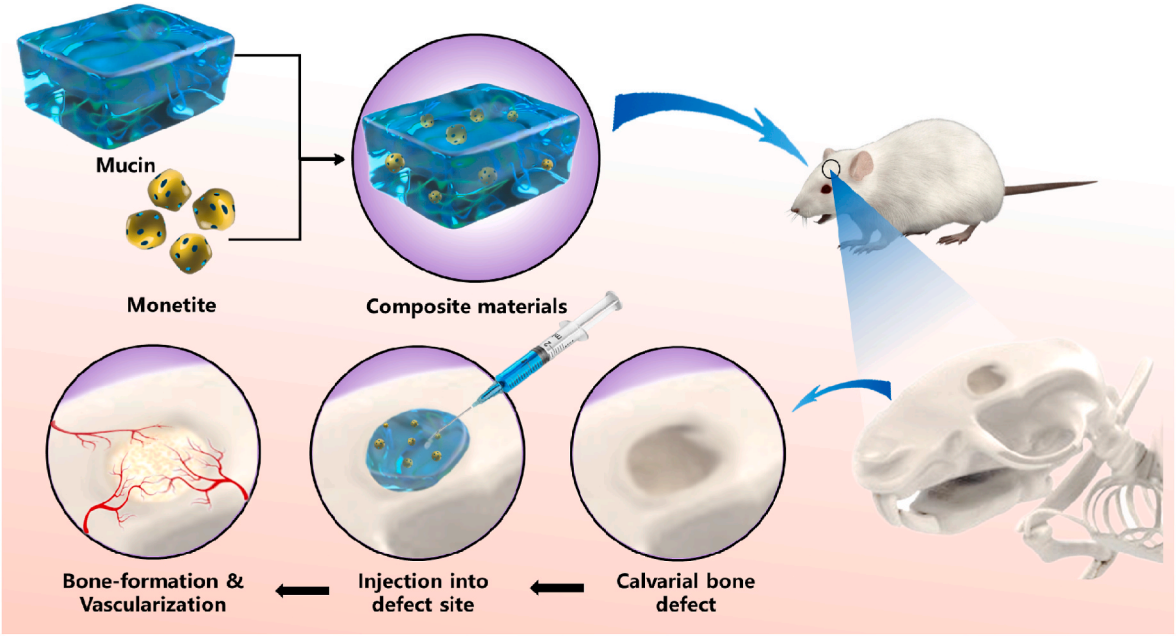

Scheme 1. The mucin-monetite hydrogel was engineered and its early osteoimmunomodulation was investigated using a rat critical-size calvarial bone defect model. The early osteoimmunomodulation enhanced early angiogenesis and ultimately promoted fracture healing.

osteoimmunomodulatory activity of monetite-based biomaterials remains unknown. The interplay between the immune response and bone reconstruction has been validated, and various strategies have been applied to enhance the osteoimmunomodulatory effect of the bioceramics. Mucin hydrogels, which possess good immunomodulating capacity, have great potential to augment the osteogenic properties of monetite through early osteoimmunomodulation. Therefore, it is our interest to investigate the possibility of using monetite-mucin composite to accelerate bone fracture healing. To prepare porous nanostructured monetite granules, we transformed porous brushite cement in the presence of NH^{4+} at 90°C, following our previous report with slight modification [39]. The porous structure of the monetite granules was confirmed by micro-CT (Fig. 1A). The complete conversion of brushite cement to monetite was confirmed by X-ray diffraction (XRD), as the peaks were consistent with the standard diffraction pattern of monetite (Fig. 1B). Mucin gels were obtained by mixing tetrazine (Tz) or norbornene (Nb)-modified bovine submaxillary mucins (BSMs) solutions (2% wt/v, 1:1 ratio (v:v)) through an inverse electron demand Diels–Alder cycloaddition reaction, as previously reported [31]. To prepare the mucin gel-monetite granule composite materials, we mixed an equal volume of monetite granules in BSM-Tz and BMS-Nb suspension (0.12 g monetite granules per 200 μL BSM-Tz and BSM-Nb solution). The monetite granules had a plate-like nanostructure, and the modification of the monetite granules by interconnected mucin hydrogels in the gel-monetite granule hybrid materials was confirmed by scanning electron microscopy (SEM) (Fig. 1C and D).

Calvarial bone defects of 5.0 mm in diameter, which are considered critical-size defects [46,47], were created in rats to assess the osteoimmunomodulation and osteogenesis of the composite materials (M-gel (+)) compared to monetite granules alone (M-gel (-)). The mucin gel-monetite granules grafts were implanted by injection, as gelation occurs only after 5 min, when the gelling components were mixed. There was a significantly lower amount of $CD80^{-}$and iNOS-expressing macrophages (M1) and a higher amount of CD163-and CD206-expressing macrophages (M2) in the explants of the M-gel (+) grafts than in those of the M-gel (-) grafts at weeks 1 and 2 (Fig. 2A and B and Fig. S1). Interestingly, we observed a decrease in CD80 and iNOS signals and an increase in CD163 and CD206 in the grafts from week 1 to week 2 (Fig. S2). M1 macrophages are only required for the initial debridement of tissues, and their prolonged presence might result in chronic inflammation and impair tissue healing [48]. M2 macrophages can produce regenerative factors such as osteogenic and angiogenic molecules, thus promoting neobone formation and revascularization [22]. CD206-expressing macrophages (M2a) express abundant platelet-derived growth factor type BB and promote the formation of blood vessels [49]. CD163-expressing macrophages (M2c) secrete high levels of matrix metalloproteinases 9 (MMP9) to promote vascular remodeling. In addition, the M1/M2 hybrid, which is formed when macrophages are exposed to M1-promoting stimuli followed by M2-promoting stimuli, has been shown to regulate the assembly and structure of the extracellular matrix [50]. Our results demonstrate that M-gel (+) grafts can polarize macrophages towards the M2 phenotype at an early stage of the bone healing process.

Using ELISA, cytokines secretion was assessed by examining grafts

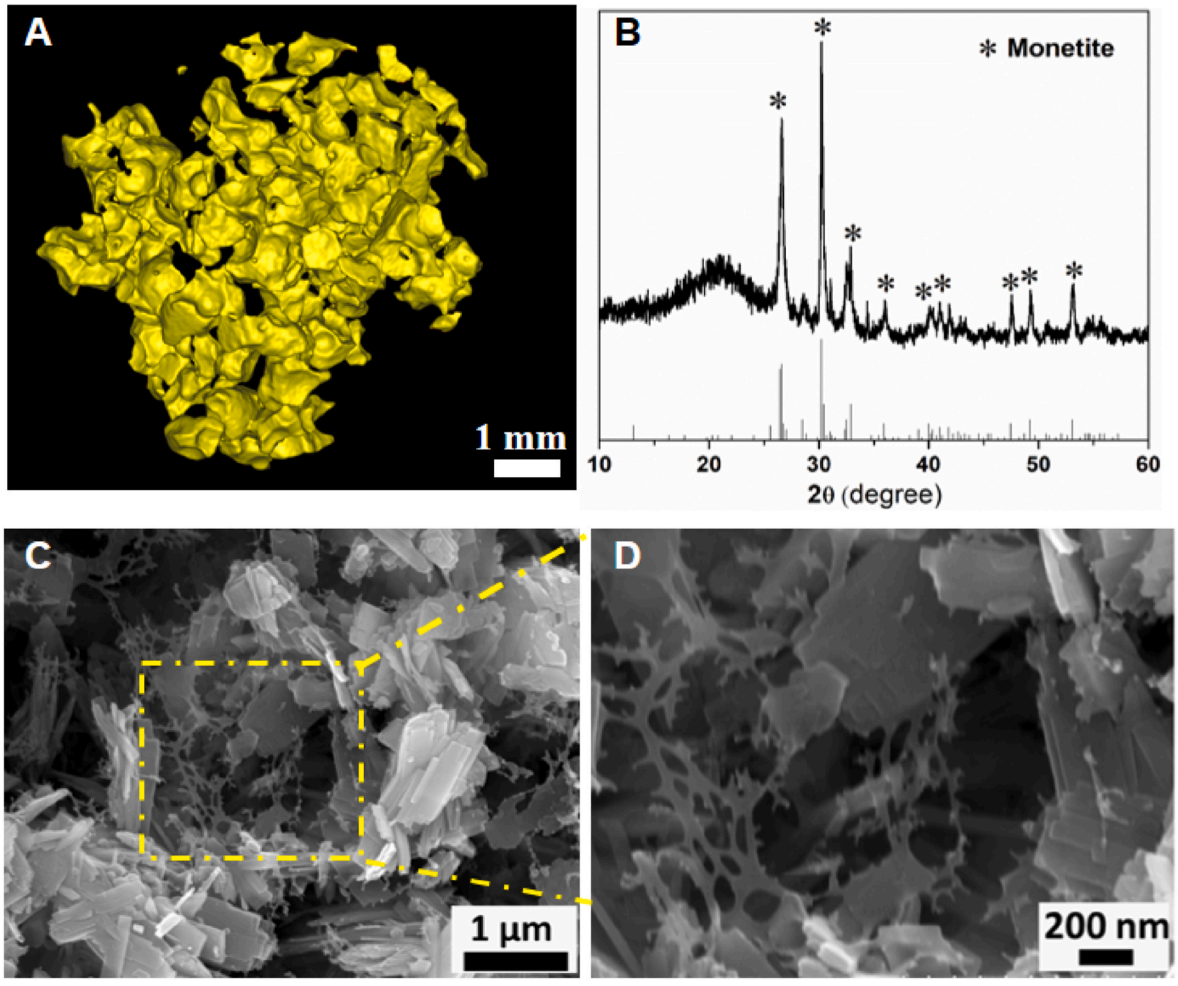

Fig. 1. Characterization of the mucin-monetite composites. (A) Micro-CT image. (B) XRD pattern. Vertical lines below the pattern are the standard diffraction pattern of monetite (PDF 00-009-0080) (C, D) SEM images.

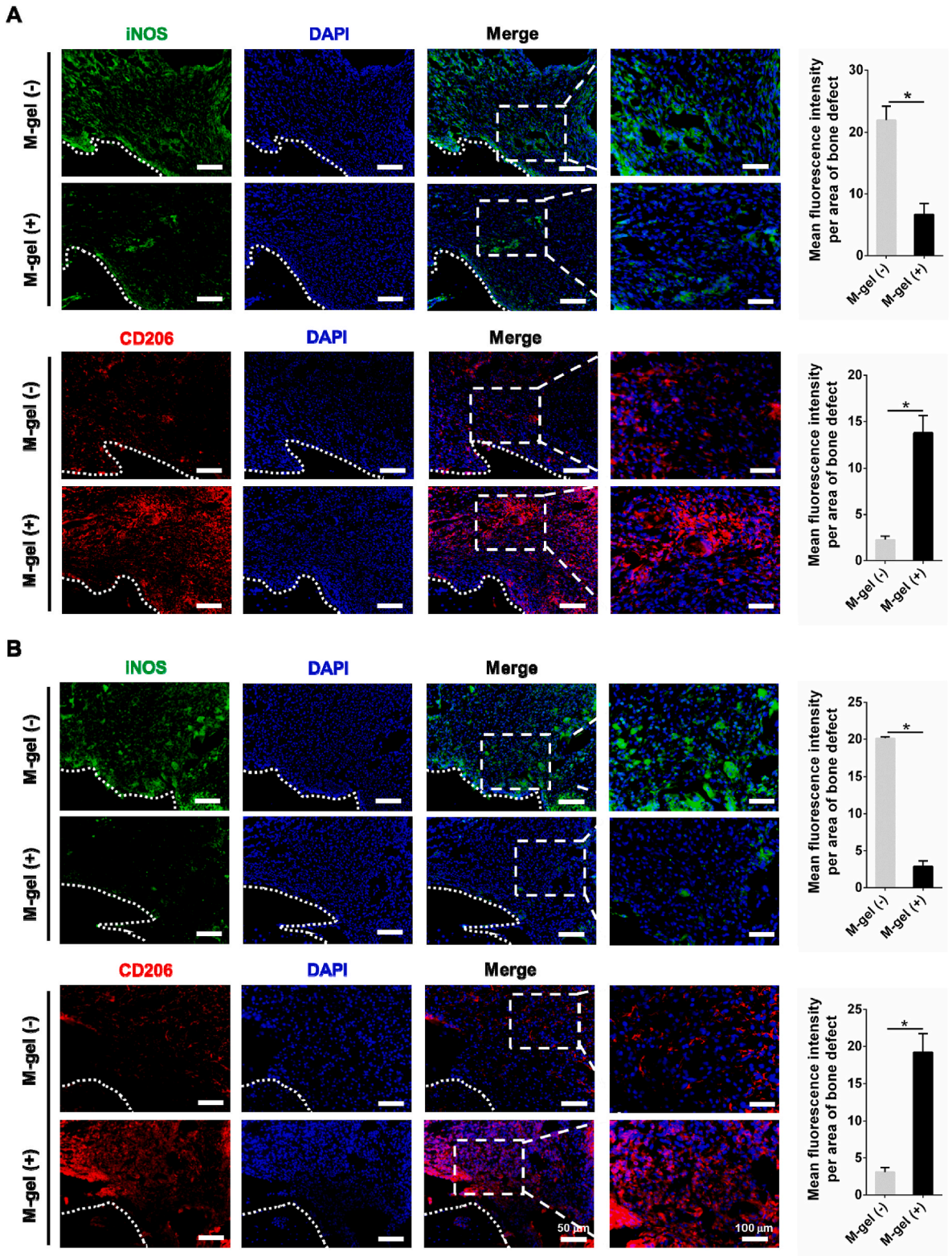

Fig. 2. Immunofluorescence evaluation of the phenotypes of the infiltrated macrophages in bone grafts. The representative images of cross sections of the grafts stained with the M1 marker (iNOS) and the M2 marker (CD206) at weeks 1 (A) and 2 (B). *, $p < 0.05$.

extracts (Fig. 3) and lavage fluids (Fig. S3) at the defect sites. The results were consistent with our previous observation that mucin hydrogels suppressed macrophage activation *in vivo* [31]. The effect of IL-8 on osteogenesis is complex. IL-8 is commonly known as a chemotactic cytokine for neutrophils and has also been shown to enhance bone regeneration via the CXCR2-mediated PI3k/Akt pathway [51]. However, several reports have indicated that IL-8 had the ability to cause bone osteolysis and resorption [52,53], and osteogenesis inhibition [54], which may be caused by its powerful pro-inflammatory effects. In this study, the IL-8 level of Muc-gel (-) group is significantly higher than that of Muc-gel (+) group (Fig. 3A). IL-1 is involved in bone resorption under pathological conditions [55]. IL-1Ra, an antagonist of

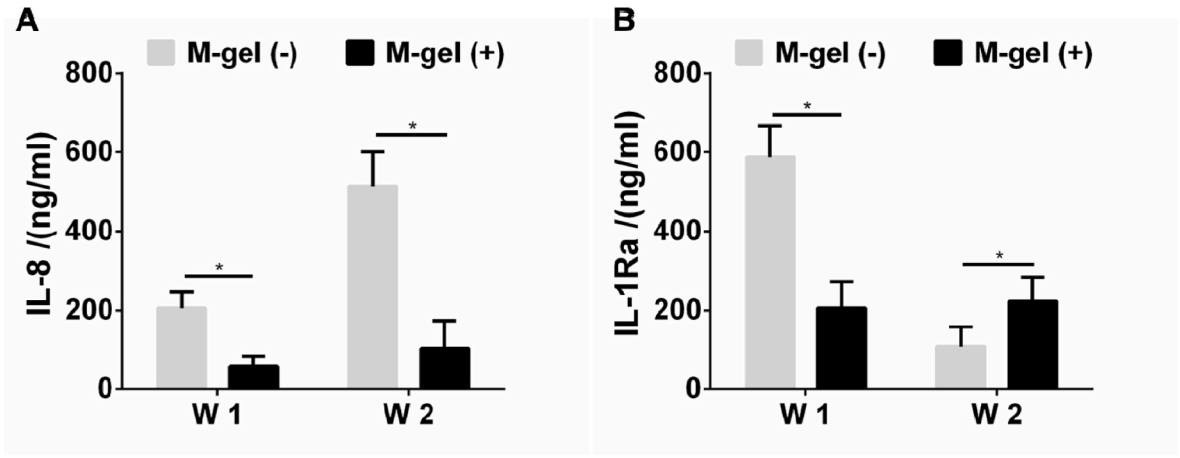

Fig. 3. The cytokines secretion by the recruited immune cells by examining grafts extracts evaluated by ELISA. Quantification of expression level of IL-8 (A) and IL-1Ra (B) and at weeks 1 and 2. *, $p < 0.05$.

IL-1, modified scaffolds to enhance osteogenesis [56]. The level of IL-1Ra in Muc-gel (+) group was significantly lower than that in Muc-gel (-) group at week 1. While the presence of mucin can sequester IL-1Ra and have a prolonged biological effect, resulting in higher level of IL-1Ra at week 2. The result is in accordance with our previous study showing that the mucin hydrogels can suppress global cytokine secretion by increasing protein inhibitor expression [31].

The markers for early osteogenesis were investigated at weeks 1 and 2. The M-gel (+) grafts induced a higher expression of Runx2 and lower expression of Sox9 (Fig. S4), and the Runx2/Sox9 ratio and ALP activity were significantly elevated compared with M-gel (-) (Fig. 4A and B). Runx2 is an important transcriptional activator essential for osteoblast differentiation and chondrocyte maturation, and Sox9 can directly interact with Runx2 to regulate its osteogenic function [57]. Runx2/Sox9 ratio can predict the osteogenic differentiation of mesenchymal stem cells [58]. ALP activity is one of the phenotypic markers of osteoblasts, which can directly reflect the activity or function of osteoblasts. Thus, our results suggested that M-gel (+) grafts promoted early osteogenesis.

Early angiogenesis was examined in the M-gel (+) and M-gel (-) grafts at weeks 1 and 2. The expression of CD31, α- SMA, and factor XIII was significantly higher in the M-gel (+) grafts than in the M-gel (-) grafts (Fig. 5A, B, C). CD31 is an essential marker for vascular endothelial differentiation [59]. α-SMA is the actin isoform characteristic of vascular smooth muscle cells [60]. Factor XIII stimulates the formation of new vessels by participating in the final step of the coagulation cascade [61]. The intensive staining of α-SMA and Factor XIII in the M-gel (+) grafts indicated the formation of mature blood vessels, showing the important role of mucin in early angiogenesis. Moreover, a higher number of blood vessels was induced in the M-gel (+) grafts than in the M-gel (-) grafts (Fig. S5). Our finding of early angiogenesis is consistent with a higher presence of M2a and M2c macrophages in the M-gel (+) grafts, which promote angiogenesis.

The entire skull was harvested, and the formation of neobone by the M-gel (+) and M-gel (-) grafts at weeks 6 and 12 were examined to evaluate the bone healing effect of the composites. Significantly higher bone volume was observed in mice implanted with M-gel (+) than in the M-gel (-) grafts and in the control group (Fig. 6A and B). Moreover, the volume of neobone doubled in the M-gel (+) group from week 6 compared to week 12 (Fig. 6B). However, the increase in neo-bone volume in the M-gel (-) group from week 6 to week 12 was significantly lower. These results demonstrated the superior regeneration of neobone tissue by M-gel (+) grafts compared to M-gel (-) grafts. In addition, representative cross-sections stained with Hematoxylin and Eosin (H&E) and Masson's trichrome showed that neobone induced by M-gel (+) had more mineralized bone with abundant osteoblasts than that induced by M-gel (-) at weeks 6 and 12 (Fig. 6C and D). Moreover, more mature bone were observed in the defect site induced by M-gel (+)

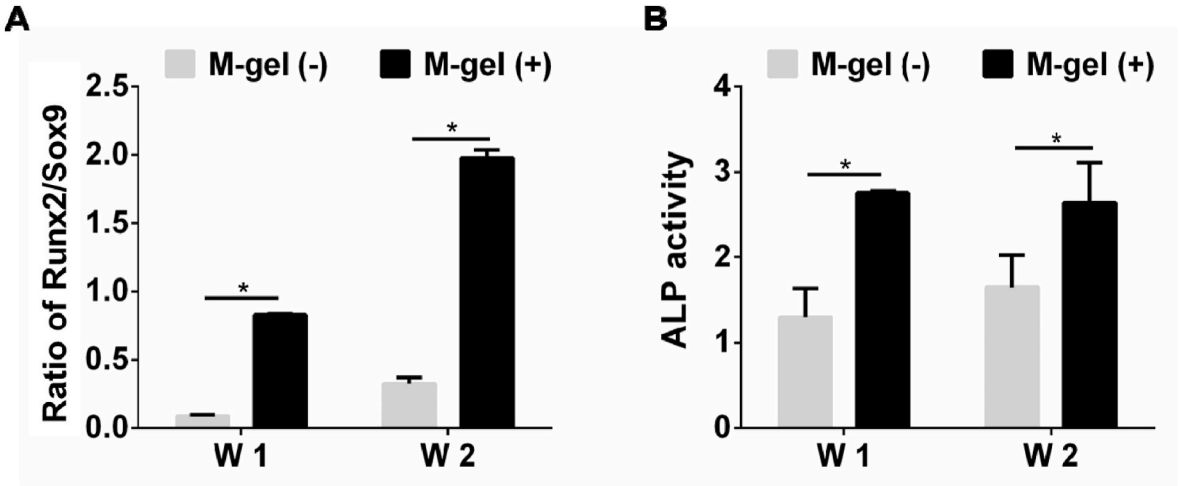

Fig. 4. Early osteogenesis by M-gel (+) and M-gel (-) grafts at weeks 1 and 2. The expression of Runx2 and Sox9 was examined by immunofluorescence. Quantification of the expression level of was performed using ImageJ. (A) The ratio of Runx2/Sox9. (B) ALP activity on extracts from explanted grafts. *, $p < 0.05$.

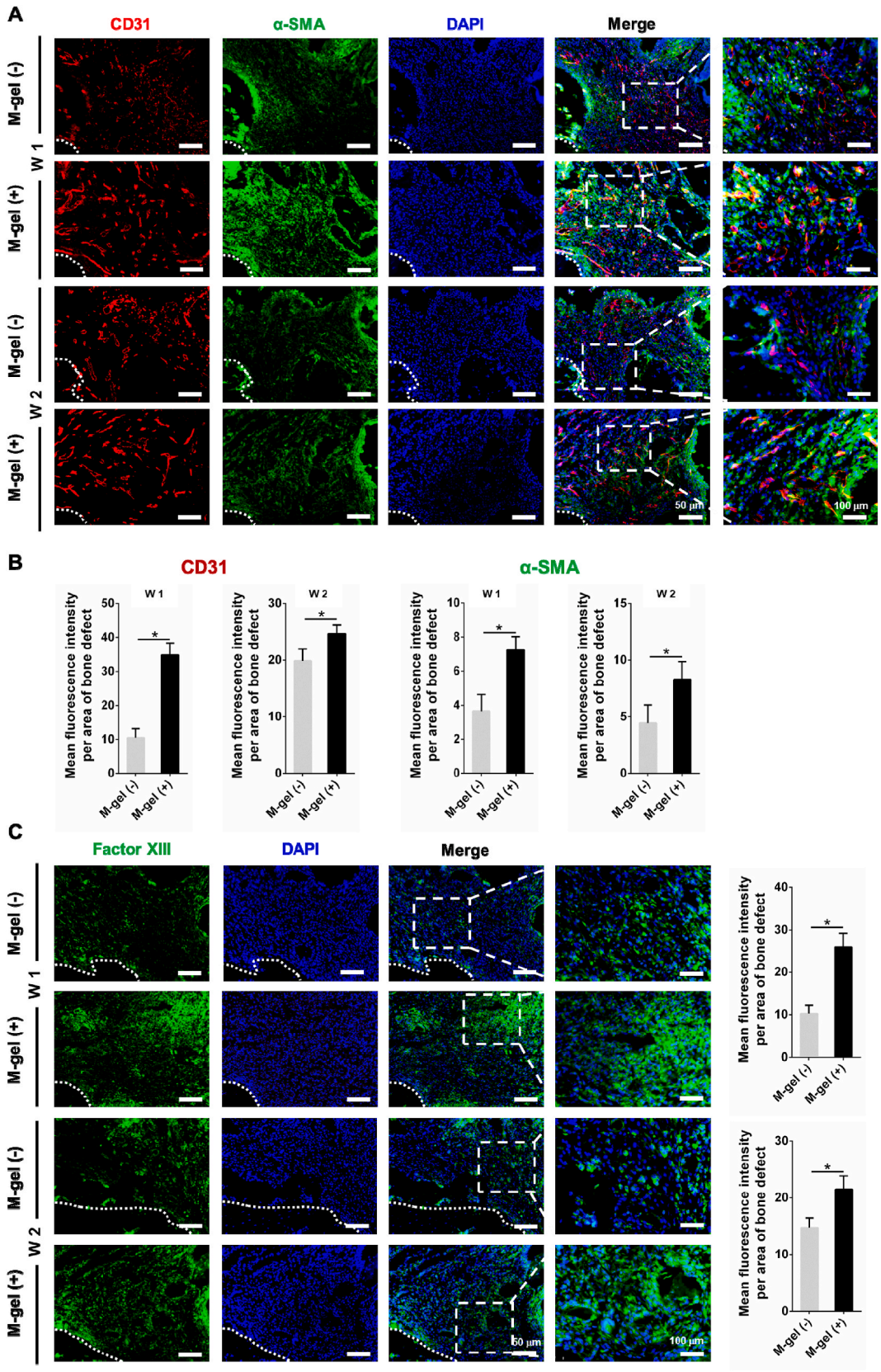

Fig. 5. Immunofluorescence evaluation of early angiogenesis in the M-gel (+) and M-gel (-) grafts at weeks 1 and 2. (A) The representative images of cross sections of the grafts stained with CD31 and α-SMA. (B) Quantification of the expression level of CD31 and α-SMA. (C) The representative images of cross sections of the grafts stained with factor XIII. *, $p < 0.05$.

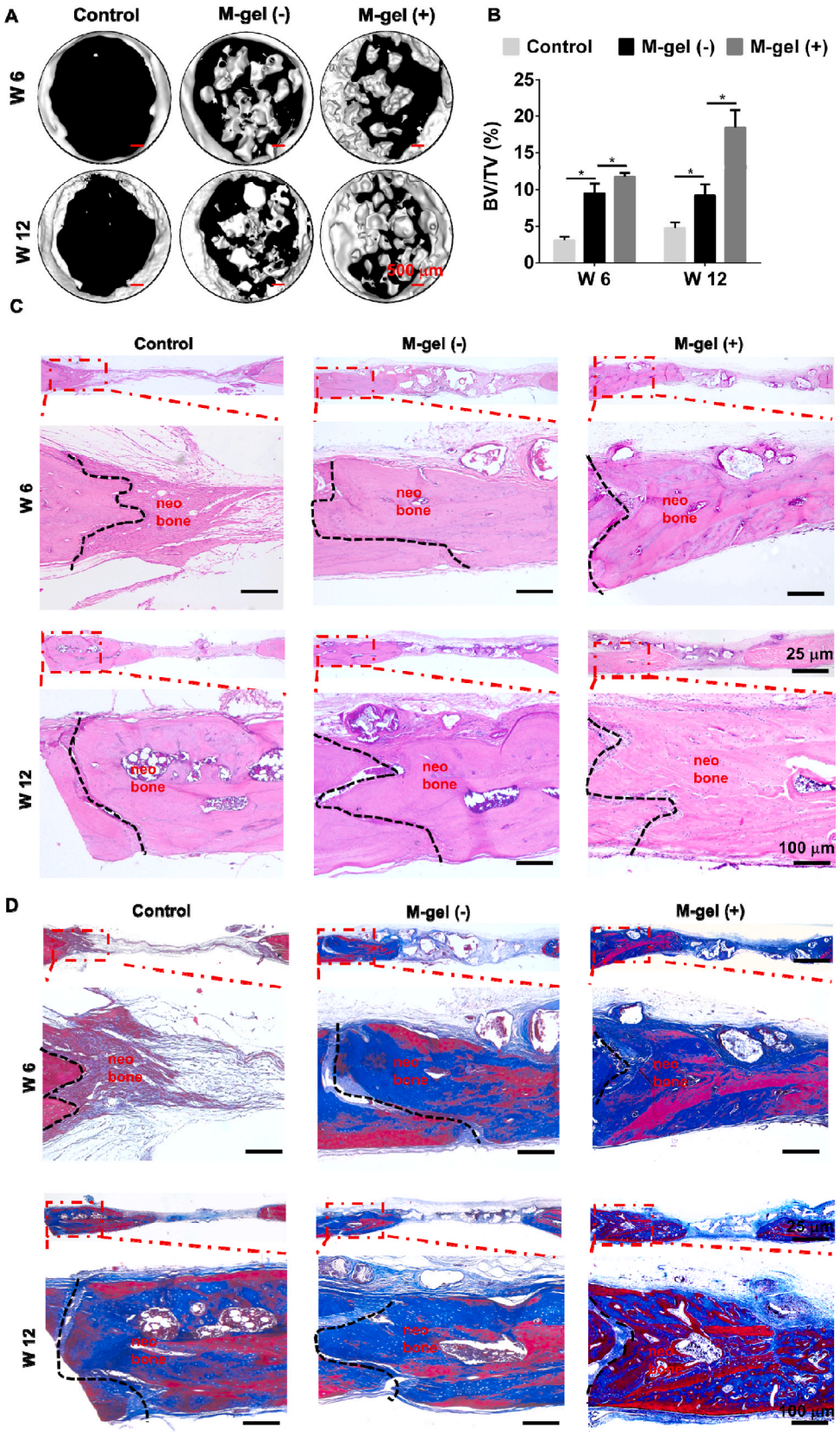

Fig. 6. Neobone formation of composite constructs in the rat calvarial defects at weeks 6 and 12 after implantation. (A) The representative images of the 3D construction from micro-CT, scale bar = 500 μm. (B) BV/TV values measured by micro-CT analysis of the neobone. (C, D) Representatives cross sections of the histological evaluation of neobone tissue at weeks 6 and 12 by H&E and Masson's trichrome staining, scale bar = 25 and 100 μm *, $p < 0.05$.

grafts, as shown by the red staining in Masson's trichrome staining at weeks 6 and 12 (Fig. 6D). This result confirmed that M-gel (+) grafts have a distinct advantage over M-gel (-) grafts in promoting bone healing.

Cross sections of the neobone harvested at weeks 6 and 12 were examined for osteopontin (OPN) expression and collagen type 1 (Col-1). The neobone induced by M-gel (+) grafts showed significantly higher expression of OPN than M-gel (-) and the control group at weeks 6 and 12 (Fig. 7A). Moreover, M-gel (+) grafts induced significantly higher expression of Col-1 compared with M-gel (-) grafts and the control group at weeks 6 and 12, especially at week 12 (Fig. 7B). OPN is the most abundant non-collagen extracellular sialylated glycoprotein in bone tissue. It is produced by osteoclasts, osteoblasts, and mesenchymal stem cells. OPN is known to directly control Col-1 production and vascularization in bone [62], interacts with integrin, and induces osteogenic differentiation of mesenchymal stem cells [63]. Thus, the result suggested that the higher expression of OPN in the neobone induced by M-gel (+) grafts at week 6 contributed to the increased deposition of Col-1 at week 12 (Fig. 7).

Neovasculature formation in the neobone harvested at weeks 6 and 12 was assessed by staining with an endothelial cell marker of CD31. Compared with the M-gel (-) grafts and the control group, increased vascularization was observed in the neobone induced by M-gel (+) grafts, as indicated by a higher expression of CD31 and the presence of vascular lumens with larger diameters surrounded by CD31-positive endothelial cells (Fig. 7C). Only few microvessels were observed in the neobone induced by M-gel (-) and in the control group. Bone is a highly vascularized tissue, and the capacity of the bone graft to induce neovascularization in the neobone is vital for engraftment. The neoblood vessels in neobone contribute to oxygen and nutrient supply and directly supply stem cells and osteoblast progenitors, which further promotes bone growth [64,65].

The chemical differences of the neobone were examined using a non-contact chemical technique, O-PTIR (Optical photothermal IR)

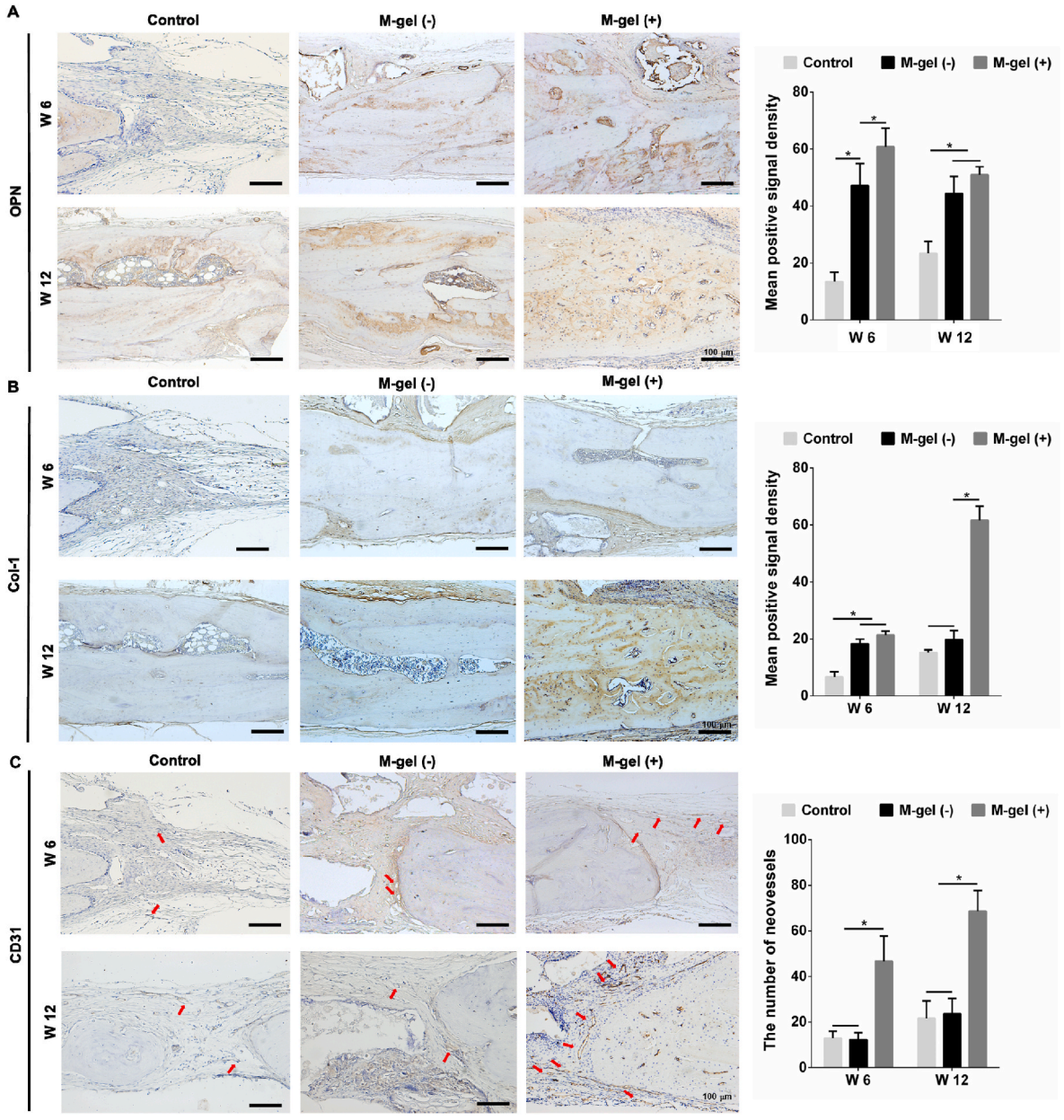

Fig. 7. Immunohistochemistry evaluation of the neobone induced by M-gel (+) and M-gel (-) grafts at weeks 6 and 12. The representative images of cross sections of the neobone of the expression of osteopontin (OPN) (A), collagen type 1 (Col-1) (B), and CD31 (C), respectively. *, $p < 0.05$.

microscopy [66,67]. High-resolution IR optical and ratio images of neobone induced by M-gel (+) and M-gel (-) grafts were acquired at different locations to visualize the phosphates (1030-1080 cm^{-1}) and amides (1541 and 1653 cm^{-1}) (Fig. 8A and B). The images showed much higher amount and broader distributions of minerals in M-gel (+) grafts. The prominent IR absorbance band at 1037-1080 cm^{-1} (phosphate) in the neobone induced by M-gel (+) grafts confirmed the enhanced biomineralization. Peaks of amide I at 1653 cm^{-1} and amide II at 1541 cm^{-1} were also predominant in the neobone induced by M-gel (+) grafts, indicating better bone formation at the defect site (Fig. 8C and D). With this technology, IR spectra in the submicron range can be obtained without contact and independent of surface roughness [66,67]. The results highlighted that O-PTIR was a valuable tool for evaluating the chemical differences in detail of the neobone.

3. Conclusion

In conclusion, our study highlighted that early osteoimmunomodulation by mucin-monetite hydrogels resulted in superior neobone formation and maturation. Moreover, we showed the composite materials induced a higher M2 phenotype than the monetite granules alone at weeks 1 and 2. Furthermore, we demonstrated higher OPN expression at week 6, which may contribute to higher Col-1 expression at week 12 in the neobone induced by the hybrid materials. Ultimately, we observed the abundant formation of neoblood vessels in the neobones induced by the composite materials. In addition, OPTIR results demonstrated enhanced signal of inorganic and organic contents *in situ* of the neobone induced by hybrid materials than monetite granules alone at week 12. Therefore, we demonstrated the potential of integrating the immunomodulatory role of mucin hydrogels into osteogenic monetite granules, which can enhance bone healing.

4. Materials and methods

4.1. Materials

Amine-modified tetrazine (Tz) and norbornene (Nb) were purchased from Bioconjugate Technology Company and TCI Europe N.V., respectively. β-TCP was purchased from Dingan Company, and MCPM was purchased from Scharlu. All other reagents were purchased from Sigma-

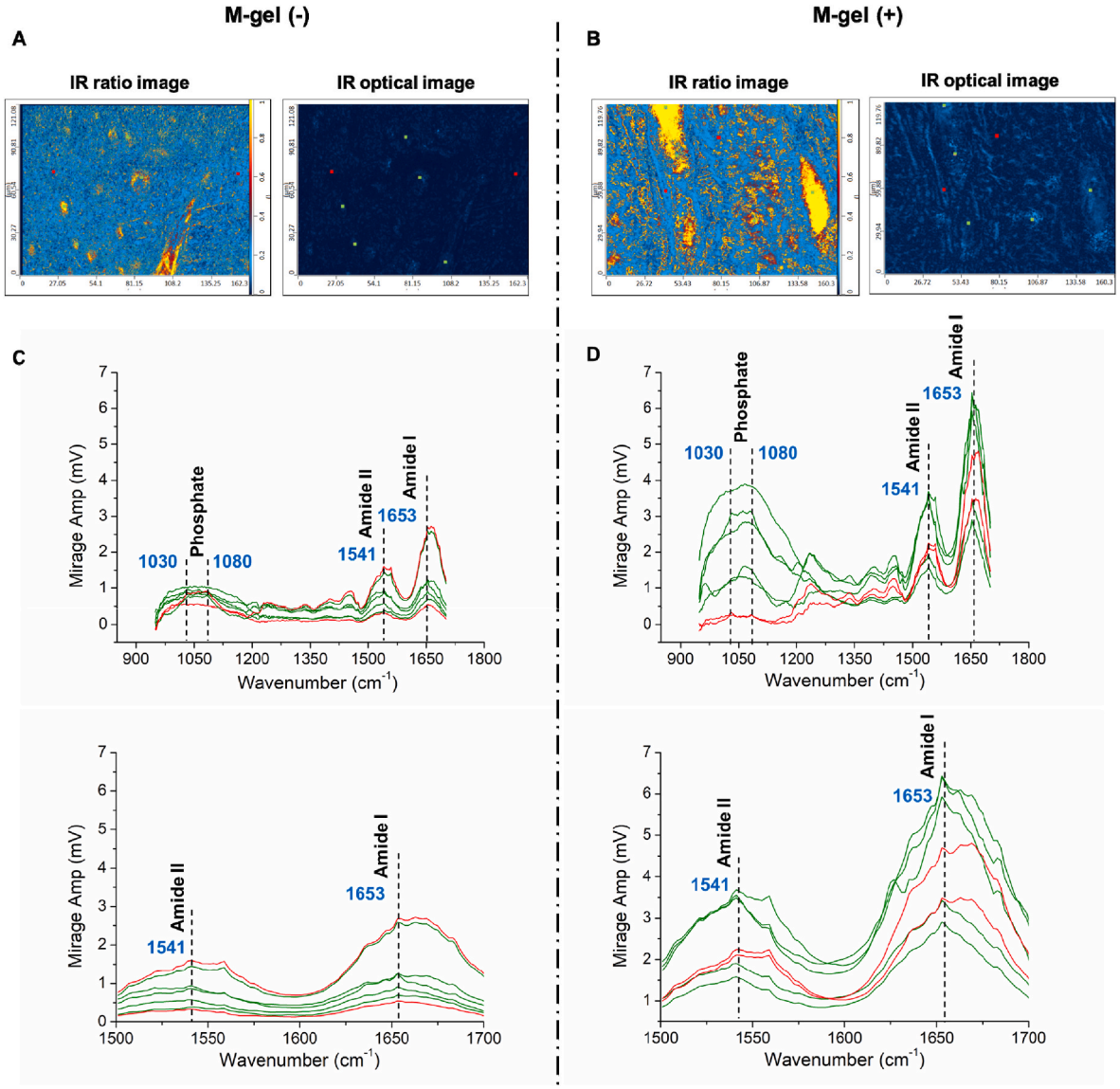

Fig. 8. Chemical differences in the neobone induced by M-gel (-) and M-gel (+) grafts at week 12 at high resolution using O-PTIR microscopy. (A, B) The IR ratio images (1037/1660 cm^{-1}) marked the mineral- and amine-rich regions (yellow/red area) in M-gel (+) and M-gel (-) grafts. (C, D) IR spectra of the markers on the IR 40x optical image. Both the yellow/red and blue spectra were analyzed for the IR spectra.

Aldrich.

4.2. Materials preparation

Paraffin wax 20 ml was dissolved at 80 °C and mixed with 50 mL polyvinyl alcohol solution with constant stirring to form paraffin microspheres. The beaker was then placed in ice water and stirred for 30 min. Subsequently, the obtained paraffin microspheres were washed with deionized water to remove the polyvinyl alcohol on the surface. The resulting particles were dried at room temperature and sieved to obtain microspheres with diameters between 200 and 600 μm. To prepare the brushite paste, a mixture of monocalcium phosphate monohydrate (MCPM) and beta-tricalcium phosphate (β-TCP) was used as the solid phase (MCPM: β-TCP = 0.45:0.55, mass ratio). Next, 1 g powder, 300 μL 0.5 M citric acid solution, and 0.7 g paraffin microspheres were thoroughly mixed and then loaded into the mold. After setting for 2 h at room temperature, the composites were placed in deionized water at 37 °C for 12 h. After demolding, the composites were vacuum dried for 24 h and crushed into granules. With constant stirring, the granules were added to the xylene solution (liquid-to-solid ratio 50 ml:1 g) for 48 h. The xylene solution was replaced every 24 h to completely dissolve the paraffin within the granules. The granules were then transferred to an anhydrous ethanol solution (liquid-to-solid ratio 50 mL:1 g) and stirred for 24 h. The solution was replaced every 8 h to completely wash out the xylene. The material was then vacuum dried and ground to obtain granules with a particle size of 0.5–1.0 mm. The obtained granules were immersed in 1 M $(NH_4)_2HPO_4$ (liquid-solid ratio 50 mL:0.5 g, pH was adjusted to 5.4 with hydrochloric acid). After stirring at 90 °C for 6 h, the granules were washed thoroughly with distilled water three times.

Mucins (BSM-Tz and BSM-Nb) were synthesized according to the previous report [31]. Briefly, bovine submaxillary mucin (BSM) was predissolved in MES buffer (0.1 m MES, 0.3 m NaCl, and pH 6.5) at a concentration of 10 mg/mL 1-ethyl-3-(3- dimethylaminopropyl) carbodiimide (EDC; 4 mmol per gram of dry mucin) and N-hydroxysuccinimide (NHS; 4 mmol per gram of dry mucin) were added to the mixture and stirred for 15 min. Thereafter, 1 mmol of tetrazine-amine (Tz) and 2 mmol of norbornene-amine (Nb) were added individually to generate the BSM tetrazine (BSM-Tz) or BSM norbornene (BSM-Nb). The mixtures were stirred overnight at 4 °C and then dialyzed for 2 days against 300×10^{-3} m NaCl and then MilliQ (MQ) water for 2 days. The samples were freeze-dried and stored at −20 °C. The gelling components were each pre-dissolved in saline at a concentration of 20 mg/mL. Monetite granules were suspended in each gelling component (0.06 mg per 200 μL). After mixing, the composites were planted into the defect area. For the M-gel (-) group, an equal amount of monetite granules was filled into the cavity.

4.3. Materials characterizations

Powder X-ray diffraction analysis (PXRD) was performed using an X-ray diffractometer (D8 Advance, Germany) with a Cu Kα radiation source (λ = 1.5418 Å), using a step size of 0.02° and an exposure time of 3 s per step. The composites were dehydrated with an ascending ethanol solution (10%, 25%, 50%, 70%, to 100%). After critical point drying, specimens were sputtered with a thin gold (Au) coating. Scanning electron microscopy (SEM) was performed using a Quanta 250 microscope with an accelerating voltage of 1.5 kV.

4.4. Rat calvarial critical-size defect model and bone cement implantation

Male Sprague-Dawley (SD) rats were purchased from the Animal Facility of Soochow University (Suzhou, China). Animal feeding and surgical procedures were performed in accordance with the NIH Guide for the Care and Use of Laboratory Animals and were approved by the Institutional Animal Care and Use Committee of Soochow University. All reagents for the hydrogels' preparation were sterile-filtered using 0.45-μm pore filters. Implants were prepared inside a cell culture laminar hood. Sixty SD rats, 10–12 weeks of age, were randomly divided into three groups (control, M-gel (-), and M-gel (+) group) and were to be harvested at 1, 2, 6, and 12 weeks after surgery. After anesthesia and disinfection with 2.5% (v/v) isoflurane and shaving the fur on the abdomen, which was sprayed with 70% (v/v) ethanol, a defect area with a diameter of 5 mm was created in the calvarium using a dental trephine burr. Then, different groups of materials were implanted into the defect area.

4.5. Immunofluorescence

At weeks 1 and 2 post-implantation, the harvested specimens were fixed in 10% formalin for 24 h, washed in 1X PBS, and decalcified at 4 °C in 10% EDTA diluted in 1X PBS for 4 weeks. Next, samples were dehydrated with 15% sucrose for 6 h, followed by dehydration with 30% sucrose overnight. Samples were then embedded in optimum cutting temperature compound (OCT, Cat. No. 4583, SAKURA, Japan), frozen in liquid nitrogen for 5 min, and stored at −80 °C. Samples were cut horizontally into 10-μm thick slices and stained with iNOS (1:500, Cat. No. ab178945, Abcam, Cambridge, UK), CD163 (1:500, Cat. No. ab182422, Abcam, Cambridge, UK), CD80 (1:200, Cat. No. A16039, ABclonal, MA, USA), CD206 (1:200, Cat. No. sc-58986, Santa Cruz, CA, USA), Sox9 (1:250, Cat. No. ab185230, Abcam, Cambridge, UK), Runx2 (1:100, Cat. No. A2851, ABclonal, MA, USA), CD31 (1:100, Cat. No. ab222783, Abcam, Cambridge, UK), α-SMA (1:200, Cat. No. sc-53142, Santa Cruz, CA, USA), and Factor VIII (1:500, Cat. No. ab275376, Abcam, Cambridge, UK) to study macrophage polarization, osteogenesis, and vascularization, respectively. The specimens were observed under a high-resolution fluorescence microscope (Zeiss Axiovert 200, Carl Zeiss Inc., Thornwood, NY, USA) with 20X and 40X objective lenses. Quantitative analysis was performed using Image J (NIH, Bethesda, MD, USA). The images that needed to be quantified were converted to grayscale, and the tissue area of interest was circled. The measurements' units, including area and mean gray level, were then selected to analyze the mean fluorescence intensity in a region of interest [68]. Neovascularization counting was performed as previously reported [66]. Round vessels were categorized as regular type 1 and long vessels as irregular type 2.

4.6. Evaluation of the expression of inflammatory factors and the activity of ALP

Whole explanted cranial tissues were incubated in 100 μL ice-cold PBS solution (1X PBS, pH 7.4, 2×10^{-3} M EDTA, and 0.5% (w/v) BSA) for 60 min. Then, the PBS solution was collected and centrifuged at 700 g for 5 min, and the supernatant was stored at −20 °C.

Explanted bone grafts were placed in 100 μL ice-cold lysis buffer (Sangon Biotech, Shanghai, China) without phosphatase inhibitors and homogenized using TissueLyser II (QIAGENE). After 72 h of incubation at 4 °C, samples were centrifuged at 12 000 g for 15 min. Supernatants were collected and stored at −20 °C.

A total of 45 μL of the supernatant was used to measure IL-8 and IL-1Ra secretion using ELISA kits, according to the manufacturer's protocol (NCM Biotech, Suzhou, China). Absorbance at 450 nm was measured using a microplate reader (BioTek, Vermont, USA).

Further, 45 μL of the supernatant was used to measure ALP activity using the ALP assay kit, according to the manufacturer's protocol (Beyotime, Shanghai, China). Absorbance at 405 nm was measured using a microplate reader (BioTek, Vermont, USA).

Micro-computed tomography analysis (Micro-CT analysis).

At weeks 6 and 12 post-surgery, the harvested specimens were fixed in 10% formalin for 24 h and washed three times in PBS. Then, the cranial tissues were examined by Micro-CT scanning (65 kV, 385 mA, and 1 mm Al filter, SkyScan 1176, SkyScan, Aartselaar, Belgium) to evaluate the three-dimensional (3D) structure of the regenerated bone

tissue within the cranial defect area. A standardized cylindrical region of interest of 5 mm in diameter was used, and data on bone volume/total volume (BV/TV) were obtained using the DataViewer software.

4.7. Optical photothermal IR (O-PTIR) analysis

O-PTIR measurements were conducted using a mIRage IR + Raman microscope (Photothermal Spectroscopy Corp.). The spectra were collected in reflection mode (Numerical Aperture: 40 × 0.78, Working Distance: 8.3 mm, Field of View: 165 mm × 125 mm) using a Schwarzschild-type Cassegrain reflective objective. A tunable pulsed quantum cascade laser with a pulse rate of 100 kHz and pulse width between 40 and 500 ns was used as a pump IR source. The probe light was a 1–200 mW continuous wave 532 nm diode-pumped solid-state laser.

4.8. Histological evaluation

The harvested specimens were fixed in 10% formalin for 24 h and decalcified in 10% EDTA diluted in 1X PBS for 4 weeks at 4 °C. The cranial tissues were then washed in PBS and dehydrated with gradient alcohol before being processed for paraffin embedding. The specimens were cut horizontally into 5-μm thick slices and then deparaffinized and rehydrated for hematoxylin, eosin (H&E), and Masson's trichrome staining. The slides were then dehydrated and mounted with coverslips. Images were acquired using a Zeiss microscope with 2.5X and 10X objective lenses (Zeiss Axiovert 200, Carl Zeiss Inc., Thornwood, NY, USA).

4.9. Immunohistochemical analysis

The harvested specimens were fixed in 10% formalin for 24 h, washed three times in 1X PBS and decalcified in 10% EDTA diluted in 1X PBS for 4 weeks at 4 °C. Then, the cranial tissues were washed in PBS and dehydrated with gradient alcohol before being processed for paraffin embedding. The specimens were cut horizontally into 5-μm thick slices and then deparaffinized and rehydrated for immunohistochemical analysis. Antigen retrieval was performed in citrate antigen retrieval solution (Beyotime, Shanghai, China), followed by incubation in 3% (v/v) hydrogen peroxide. Sections were blocked in goat serum (5%) diluted in PBS for 1 h at room temperature and then incubated with primary rabbit primary antibodies: CD31 (1:1000, Cat. No. ab182981, Abcam, Cambridge, UK), OPN (1:200, Cat. No. GTX31886, GeneTex, CA, USA), Col-1 (1:200, Cat. No. ab6308, Abcam, Cambridge, UK), or rabbit IgG (1:400, Cat. No. A7016, Beyotime, Shanghai, China) in a humidified chamber overnight at 4 °C. Slides were then incubated with HRP-labeled goat anti-rabbit secondary antibody (1:50, Cat. No. A0208, Beyotime, Shanghai, China) diluted in PBS. After visualization with diaminobenzidine-based peroxidase substrate (DAB) and counter-staining with hematoxylin, images were acquired using a Zeiss microscope with 10X objective lens (Zeiss Axiovert 200, Carl Zeiss Inc., Thornwood, NY, USA). Immunohistochemical staining results were analyzed with a semiquantitative method [69] using Image J (NIH, Bethesda, MD, USA). The images were opened, color deconvolution was clicked, and DAB was selected. The images were converted into three different images, and the image of color 2 represented only the DAB staining. After selecting the threshold option, the brown image was converted to a black and white image, and the maximum threshold was then adjusted to remove the background signal without removing the proper DAB signal. The neobone area was circled, followed by the selection of measurement settings, including area and average gray value, to quantify the DAB signal.

4.10. Statistics analysis

All data were expressed as the mean ± standard deviation (SD). Statistical analyses were performed using ANOVA followed by Tukey's post hoc analysis (GraphPad Prism 9.0, USA). The significant differences are marked with asterisks where applicable, and "*" indicate p-values <0.05.

Ethics approval and consent to participate

The experimental protocol was established, according to the NIH Guide for the Care and Use of Laboratory Animals and were approved by the Institutional Animal Care and Use Committee of Soochow University.

CRediT authorship contribution statement

Song Chen: Conceptualization, Methodology, Investigation, Writing – original draft, Writing – review & editing, Project administration, Funding acquisition. **Huan Wang:** Conceptualization, Methodology, Investigation, Writing – original draft, Writing – review & editing. **Dachuan Liu:** Investigation, Formal analysis. **Jianzhong Bai:** Investigation. **Håvard Jostein Haugen:** Methodology, Writing – review & editing. **Bin Li:** Conceptualization, Supervision, Funding acquisition, Project administration, Writing – review & editing. **Hongji Yan:** Conceptualization, Methodology, Writing – original draft, Writing – review & editing, Project administration, Funding acquisition.

Declaration of competing interest

The authors declare that they have no known competing financial interests or personal relationships that could appear to influence the work reported in this paper.

Acknowledgment

The authors gratefully acknowledge financial support from the National Natural Science Foundation of China (81925027, 82002275, 32271421), Natural Science Foundation of the Jiangsu Higher Education Institutions of China (20KJB430041), the Priority Academic Program Development of Jiangsu Higher Education Institutions, the Swedish Foundation for Strategic Research (Grant No. FFL15-0072), KTH Lifescience platform grant 2021, and Norweigian Research Council (331752). The authors thank Dr. Thomas Crouzier for the discussion. Antti Kalanti, Eoghan Dillon and Dr Mustafa Kansiz are acknowledged for the measurement of O-PTIR.

Appendix A. Supplementary data

Supplementary data to this article can be found online at https://doi.org/10.1016/j.bioactmat.2023.01.022.

References

[1] G.S. Shi, Y.Y. Li, Y.P. Luo, J.F. Jin, Y.X. Sun, L.Z. Zheng, Y.X. Lai, L. Li, G.H. Fu, L. Qin, S.H. Chen, Bioactive PLGA/tricalcium phosphate scaffolds incorporating phytomolecule icaritin developed for calvarial defect repair in rat model, J Orthop Translat 24 (2020) 112–120.
[2] J.M. Townsend, G. Sali, H.B. Homburg, N.T. Cassidy, M.E. Sanders, K.M. Fung, B. T. Andrews, R.J. Nudo, B.N. Bohnstedt, M.S. Detamore, Thiolated bone and tendon tissue particles covalently bound in hydrogels for in vivo calvarial bone regeneration, Acta Biomater. 104 (2020) 66–75.
[3] J. Li, F. Cao, B. Wu, J. Yang, W. Xu, W. Wang, X. Wei, G. Liu, D. Zhao, Immobilization of bioactive vascular endothelial growth factor onto Ca-deficient hydroxyapatite-coated Mg by covalent bonding using polydopamine, J Orthop Translat 30 (2021) 82–92.
[4] Y. Zhang, Y. Jiang, D. Zou, B. Yuan, H.Z. Ke, W. Li, Therapeutics for enhancement of spinal fusion: a mini review, J Orthop Translat 31 (2021) 73–79.
[5] J.S. Silber, D.G. Anderson, S.D. Daffner, B.T. Brislin, J.M. Leland, A.S. Hilibrand, A. R. Vaccaro, T.J. Albert, Donor site morbidity after anterior iliac crest bone harvest for single-level anterior cervical discectomy and fusion, Spine 28 (2) (2003) 134–139 (Phila Pa 1976).

[6] E. Steijvers, A. Ghei, Z. Xia, Manufacturing artificial bone allografts: a perspective, Biomater Transl 3 (1) (2022) 65–80.
[7] H.J. Haugen, S.P. Lyngstadaas, F. Rossi, G. Perale, Bone grafts: which is the ideal biomaterial? J. Clin. Periodontol. 46 (Suppl 21) (2019) 92–102.
[8] B.A. Alman, S.P. Kelley, D. Nam, Heal thyself: using endogenous regeneration to repair bone, Tissue Eng. B Rev. 17 (6) (2011) 431–436.
[9] S. Chen, H. Wang, V.L. Mainardi, G. Talo, A. McCarthy, J.V. John, M.J. Teusink, L. Hong, J. Xie, Biomaterials with structural hierarchy and controlled 3D nanotopography guide endogenous bone regeneration, Sci. Adv. 7 (31) (2021), eabg3089.
[10] Y. Peng, J. Li, H. Lin, S. Tian, S. Liu, F. Pu, L. Zhao, K. Ma, X. Qing, Z. Shao, Endogenous repair theory enriches construction strategies for orthopaedic biomaterials: a narrative review, Biomater Transl 2 (4) (2021) 343–360.
[11] Y. Xie, C. Hu, Y. Feng, D. Li, T. Ai, Y. Huang, X. Chen, L. Huang, J. Tan, Osteoimmunomodulatory effects of biomaterial modification strategies on macrophage polarization and bone regeneration, Regen Biomater 7 (3) (2020) 233–245.
[12] L. Ouyang, J. Cao, Q. Dai, D. Qiu, New insight of immuno-engineering in osteoimmunomodulation for bone regeneration, Regen Ther 18 (2021) 24–29.
[13] J. Lee, H. Byun, S.K. Madhurakkat Perikamana, S. Lee, H. Shin, Current advances in immunomodulatory biomaterials for bone regeneration, Adv Healthc Mater 8 (4) (2019), e1801106.
[14] M. Maruyama, C. Rhee, T. Utsunomiya, N. Zhang, M. Ueno, Z. Yao, S.B. Goodman, Modulation of the inflammatory response and bone healing, Front. Endocrinol. 11 (2020) 386.
[15] M.M. Stevens, R.P. Marini, D. Schaefer, J. Aronson, R. Langer, V.P. Shastri, In vivo engineering of organs: the bone bioreactor, Proc. Natl. Acad. Sci. U. S. A. 102 (32) (2005) 11450–11455.
[16] C. Schlundt, T. El Khassawna, A. Serra, A. Dienelt, S. Wendler, H. Schell, N. van Rooijen, A. Radbruch, R. Lucius, S. Hartmann, G.N. Duda, K. Schmidt-Bleek, Macrophages in bone fracture healing: their essential role in endochondral ossification, Bone 106 (2018) 78–89.
[17] C. Montoya, Y. Du, A.L. Gianforcaro, S. Orrego, M. Yang, P.I. Lelkes, On the road to smart biomaterials for bone research: definitions, concepts, advances, and outlook, Bone Res 9 (1) (2021) 12.
[18] T. Li, M. Peng, Z. Yang, X. Zhou, Y. Deng, C. Jiang, M. Xiao, J. Wang, 3D-printed IFN-gamma-loading calcium silicate-beta-tricalcium phosphate scaffold sequentially activates M1 and M2 polarization of macrophages to promote vascularization of tissue engineering bone, Acta Biomater. 71 (2018) 96–107.
[19] A. Mansour, L. Abu-Nada, H. Al-Waeli, M.A. Mezour, M.N. Abdallah, J.M. Kinsella, J. Kort-Mascort, J.E. Henderson, J.L. Ramirez-Garcialuna, S.D. Tran, O.A. Elkashty, A. Mousa, A.A. El-Hadad, D. Taqi, F. Al-Hamad, O. Alageel, M.T. Kaartinen, F. Tamimi, Bone extracts immunomodulate and enhance the regenerative performance of dicalcium phosphates bioceramics, Acta Biomater. 89 (2019) 343–358.
[20] M. Rahmati, S. Stotzel, T.E. Khassawna, K. Iskhahova, D.C. Florian Wieland, B. Zeller Plumhoff, H.J. Haugen, Early osteoimmunomodulatory effects of magnesium-calcium-zinc alloys, J. Tissue Eng. 12 (2021), 20417314211047100.
[21] M. Wang, Y. Yu, K. Dai, Z. Ma, Y. Liu, J. Wang, C. Liu, Improved osteogenesis and angiogenesis of magnesium-doped calcium phosphate cement via macrophage immunomodulation, Biomater. Sci. 4 (11) (2016) 1574–1583.
[22] J.M. Sadowska, M.P. Ginebra, Inflammation and biomaterials: role of the immune response in bone regeneration by inorganic scaffolds, J. Mater. Chem. B 8 (41) (2020) 9404–9427.
[23] P. Humbert, M.A. Brennan, N. Davison, P. Rosset, V. Trichet, F. Blanchard, P. Layrolle, Immune modulation by transplanted calcium phosphate biomaterials and human mesenchymal stromal cells in bone regeneration, Front. Immunol. 10 (2019) 663.
[24] G. Petrou, T. Crouzier, Mucins as multifunctional building blocks of biomaterials, Biomater. Sci. 6 (9) (2018) 2282–2297.
[25] M.E. Johansson, G.C. Hansson, Immunological aspects of intestinal mucus and mucins, Nat. Rev. Immunol. 16 (10) (2016) 639–649.
[26] J. Chin-Hun Kuo, J.G. Gandhi, R.N. Zia, M.J. Paszek, Physical biology of the cancer cell glycocalyx, Nat. Phys. 14 (7) (2018) 658–669.
[27] V.P. Bhavanandan, J.D. Hegarty, Identification of the mucin core protein by cell-free translation of messenger RNA from bovine submaxillary glands, J. Biol. Chem. 262 (12) (1987) 5913–5917.
[28] M. Shan, M. Gentile, J.R. Yeiser, A.C. Walland, V.U. Bornstein, K. Chen, B. He, L. Cassis, A. Bigas, M. Cols, L. Comerma, B. Huang, J.M. Blander, H. Xiong, L. Mayer, C. Berin, L.H. Augenlicht, A. Velcich, A. Cerutti, Mucus enhances gut homeostasis and oral tolerance by delivering immunoregulatory signals, Science 342 (6157) (2013) 447–453.
[29] A. Varki, P. Gagneux, Multifarious roles of sialic acids in immunity, Ann. N. Y. Acad. Sci. 1253 (2012) 16–36.
[30] H. Yan, M. Melin, K. Jiang, M. Trossbach, B. Badadamath, K. Langer, B. Winkeljann, O. Lieleg, J. Hong, H.N. Joensson, T. Crouzier, Immune-modulating mucin hydrogel microdroplets for the encapsulation of cell and microtissue, Adv. Funct. Mater. 31 (42) (2021), 2105967.
[31] H. Yan, C. Seignez, M. Hjorth, B. Winkeljann, M. Blakeley, O. Lieleg, M. Phillipson, T. Crouzier, Immune-informed mucin hydrogels evade fibrotic foreign body response in vivo, Adv. Funct. Mater. 29 (46) (2019), 1902581.
[32] H. Yan, M. Hjorth, B. Winkeljann, I. Dobryden, O. Lieleg, T. Crouzier, Glyco-modification of mucin hydrogels to investigate their immune activity, ACS Appl. Mater. Interfaces 12 (17) (2020) 19324–19336.
[33] K. Jiang, H. Yan, C. Rickert, M. Marczynski, K. Sixtensson, F. Vilaplana, O. Lieleg, T. Crouzier, Modulating the bioactivity of mucin hydrogels with crosslinking architecture, Adv. Funct. Mater. 31 (10) (2021), 2008428.
[34] A. Barba, A. Diez-Escudero, Y. Maazouz, K. Rappe, M. Espanol, E.B. Montufar, M. Bonany, J.M. Sadowska, J. Guillem-Marti, C. Ohman-Magi, C. Persson, M. C. Manzanares, J. Franch, M.P. Ginebra, Osteoinduction by foamed and 3D-printed calcium phosphate scaffolds: effect of nanostructure and pore architecture, ACS Appl. Mater. Interfaces 9 (48) (2017) 41722–41736.
[35] R.Z. LeGeros, Calcium phosphate-based osteoinductive materials, Chem. Rev. 108 (11) (2008) 4742–4753.
[36] Z. Sheikh, Y.L. Zhang, F. Tamimi, J. Barralet, Effect of processing conditions of dicalcium phosphate cements on graft resorption and bone formation, Acta Biomater. 53 (2017) 526–535.
[37] F. Theiss, D. Apelt, B. Brand, A. Kutter, K. Zlinszky, M. Bohner, S. Matter, C. Frei, J. A. Auer, B. von Rechenberg, Biocompatibility and resorption of a brushite calcium phosphate cement, Biomaterials 26 (21) (2005) 4383–4394.
[38] B. Kruppke, J. Farack, A.S. Wagner, S. Beckmann, C. Heinemann, K. Glenske, S. Rossler, H.P. Wiesmann, S. Wenisch, T. Hanke, Gelatine modified monetite as a bone substitute material: an in vitro assessment of bone biocompatibility, Acta Biomater. 32 (2016) 275–285.
[39] S. Chen, M. Krumova, H. Cölfen, E.V. Sturm, Synthesis of fiber-like monetite without organic additives and its transformation to hydroxyapatite, Chem. Mater. 31 (5) (2019) 1543–1551.
[40] D. Ren, Q. Ruan, J. Tao, J. Lo, S. Nutt, J. Moradian-Oldak, Amelogenin affects brushite crystal morphology and promotes its phase transformation to monetite, Cryst. Growth Des. 16 (9) (2016) 4981–4990.
[41] G. Schneider, K. Blechschmidt, D. Linde, P. Litschko, T. Korbs, E. Beleites, Bone regeneration with glass ceramic implants and calcium phosphate cements in a rabbit cranial defect model, J. Mater. Sci. Mater. Med. 21 (10) (2010) 2853–2859.
[42] F. Tamimi, J. Torres, D. Bassett, J. Barralet, E.L. Cabarcos, Resorption of monetite granules in alveolar bone defects in human patients, Biomaterials 31 (10) (2010) 2762–2769.
[43] F. Tamimi, J. Torres, C. Kathan, R. Baca, C. Clemente, L. Blanco, E. Lopez Cabarcos, Bone regeneration in rabbit calvaria with novel monetite granules, J. Biomed. Mater. Res. 87 (4) (2008) 980–985.
[44] S.J. Hollister, Porous scaffold design for tissue engineering, Nat. Mater. 4 (7) (2005) 518–524.
[45] H. Zhou, L. Yang, U. Gbureck, S.B. Bhaduri, P. Sikder, Monetite, an important calcium phosphate compound-Its synthesis, properties and applications in orthopedics, Acta Biomater. 127 (2021) 41–55.
[46] A. Vajgel, N. Mardas, B.C. Farias, A. Petrie, R. Cimoes, N. Donos, A systematic review on the critical size defect model, Clin. Oral Implants Res. 25 (8) (2014) 879–893.
[47] P.P. Spicer, J.D. Kretlow, S. Young, J.A. Jansen, F.K. Kasper, A.G. Mikos, Evaluation of bone regeneration using the rat critical size calvarial defect, Nat. Protoc. 7 (10) (2012) 1918–1929.
[48] P. Italiani, D. Boraschi, From monocytes to M1/M2 macrophages: phenotypical vs. Functional differentiation, Front. Immunol. 5 (2014) 514.
[49] D. Xu, J. Qian, X. Guan, L. Ren, K. Yang, X. Huang, S. Zhang, Y. Chai, X. Wu, H. Wu, X. Zhang, K. Yang, B. Yu, Copper-containing alloy as immunoregulatory material in bone regeneration via mitochondrial oxidative stress, Front. Bioeng. Biotechnol. 8 (2020), 620629.
[50] C.E. Witherel, K. Sao, B.K. Brisson, B. Han, S.W. Volk, R.J. Petrie, L. Han, K. L. Spiller, Regulation of extracellular matrix assembly and structure by hybrid M1/M2 macrophages, Biomaterials 269 (2021), 120667.
[51] A. Yang, Y. Lu, J. Xing, Z. Li, X. Yin, C. Dou, S. Dong, F. Luo, Z. Xie, T. Hou, J. Xu, IL-8 enhances therapeutic effects of BMSCs on bone regeneration via CXCR2-mediated PI3k/akt signaling pathway, Cell. Physiol. Biochem. 48 (1) (2018) 361–370.
[52] Y. Zhang, B. Zou, Y. Tan, J. Su, Y. Wang, J. Xu, L. Tao, H. Zhou, L. Liu, X. Li, Sinomenine inhibits osteolysis in breast cancer by reducing IL-8/CXCR1 and c-Fos/NFATc1 signaling, Pharmacol. Res. 142 (2019) 140–150.
[53] T. Morita, Y. Shima, K. Fujimoto, H. Tsuboi, Y. Saeki, M. Narazaki, A. Ogata, A. Kumanogoh, Anti-receptor activator of nuclear factor kappaB ligand antibody treatment increases osteoclastogenesis-promoting IL-8 in patients with rheumatoid arthritis, Int. Immunol. 31 (5) (2019) 277–285.
[54] L.Y. Chou, C.T. Ho, S.C. Hung, Paracrine senescence of mesenchymal stromal cells involves inflammatory cytokines and the NF-kappaB pathway, Cells 11 (20) (2022).
[55] Y.M. Lee, N. Fujikado, H. Manaka, H. Yasuda, Y. Iwakura, IL-1 plays an important role in the bone metabolism under physiological conditions, Int. Immunol. 22 (10) (2010) 805–816.
[56] Z. Julier, R. Karami, B. Nayer, Y.Z. Lu, A.J. Park, K. Maruyama, G.A. Kuhn, R. Muller, S. Akira, M.M. Martino, Enhancing the regenerative effectiveness of growth factors by local inhibition of interleukin-1 receptor signaling, Sci. Adv. 6 (24) (2020), eaba7602.
[57] G. Zhou, Q. Zheng, F. Engin, E. Munivez, Y. Chen, E. Sebald, D. Krakow, B. Lee, Dominance of SOX9 function over RUNX2 during skeletogenesis, Proc. Natl. Acad. Sci. U. S. A. 103 (50) (2006) 19004–19009.
[58] C. Loebel, E.M. Czekanska, M. Bruderer, G. Salzmann, M. Alini, M.J. Stoddart, In vitro osteogenic potential of human mesenchymal stem cells is predicted by Runx2/Sox9 ratio, Tissue Eng. 21 (1–2) (2015) 115–123.
[59] P. Lertkiatmongkol, D. Liao, H. Mei, Y. Hu, P.J. Newman, Endothelial functions of platelet/endothelial cell adhesion molecule-1 (CD31), Curr. Opin. Hematol. 23 (3) (2016) 253–259.

[60] B. Hinz, G. Celetta, J.J. Tomasek, G. Gabbiani, C. Chaponnier, Alpha-smooth muscle actin expression upregulates fibroblast contractile activity, Mol. Biol. Cell 12 (9) (2001) 2730–2741.
[61] R. Dardik, J. Loscalzo, A. Inbal, Factor XIII (FXIII) and angiogenesis, J. Thromb. Haemostasis 4 (1) (2006) 19–25.
[62] C.M. Franca, G. Thrivikraman, A. Athirasala, A. Tahayeri, L.B. Gower, L. E. Bertassoni, The influence of osteopontin-guided collagen intrafibrillar mineralization on pericyte differentiation and vascularization of engineered bone scaffolds, J. Biomed. Mater. Res. B Appl. Biomater. 107 (5) (2019) 1522–1532.
[63] Q. Chen, P. Shou, L. Zhang, C. Xu, C. Zheng, Y. Han, W. Li, Y. Huang, X. Zhang, C. Shao, A.I. Roberts, A.B. Rabson, G. Ren, Y. Zhang, Y. Wang, D.T. Denhardt, Y. Shi, An osteopontin-integrin interaction plays a critical role in directing adipogenesis and osteogenesis by mesenchymal stem cells, Stem Cell. 32 (2) (2014) 327–337.
[64] Y. Kang, S. Kim, M. Fahrenholtz, A. Khademhosseini, Y. Yang, Osteogenic and angiogenic potentials of monocultured and co-cultured human-bone-marrow-derived mesenchymal stem cells and human-umbilical-vein endothelial cells on three-dimensional porous beta-tricalcium phosphate scaffold, Acta Biomater. 9 (1) (2013) 4906–4915.
[65] F. Kang, Q. Yi, P. Gu, Y. Dong, Z. Zhang, L. Zhang, Y. Bai, Controlled growth factor delivery system with osteogenic-angiogenic coupling effect for bone regeneration, J Orthop Translat 31 (2021) 110–125.
[66] M. Rahmati, S. Stötzel, T. El Khassawna, C. Mao, A. Ali, J.C. Vaughan, K. Iskhahova, D.C. Florian Wieland, A.G. Cantalapiedra, G. Perale, F. Betge, E. P. Dillon, S.P. Lyngstadaas, H.J. Haugen, Intrinsically disordered peptides enhance regenerative capacities of bone composite xenografts, Mater. Today 52 (2022) 63–79.
[67] A.J. Wang, E.P. Dillon, S. Maharjan, K.-S. Liao, B.P. McElhenny, T. Tong, S. Chen, J. Bao, S.A. Curran, Nanocomposite interfaces: resolving nanocomposite interfaces via simultaneous submicrometer optical-photothermal infrared-Raman microspectroscopy (adv. Mater. Interfaces 5/2021), Adv. Funct. Mater. 8 (5) (2021), 2170022.
[68] M.H. Shihan, S.G. Novo, S.J. Le Marchand, Y. Wang, M.K. Duncan, A simple method for quantitating confocal fluorescent images, Biochem Biophys Rep 25 (2021), 100916.
[69] A.R. Crowe, W. Yue, Semi-quantitative determination of protein expression using immunohistochemistry staining and analysis: an integrated protocol, Bio Protoc 9 (24) (2019) e3465.